Laboratory validation of pulsed thermography in the rapid assessment of external corrosion in buried metallic utilities

Samuel Yu [a], Winnie Wai-sze Chung [a], Tom Chun-wai Lau [a], Wallace Wai-lok Lai [a], Janet Fung Chu Sham [a], Chun Yiu Ho [b]

[a] Department of Land Surveying and Geo-informatics, The Hong Kong Polytechnic University, Hong Kong

[b] The Hong Kong and China Gas Company

Abstract: This study characterized the thermal signature of wall thinning in steel pipes, a common problem that is caused by external corrosion in hostile underground environment. A model system was prepared by milling several holes of various sizes and residual thicknesses into a mild steel plate. Wall thinning was investigated using active infrared thermography. The non-defective side of the steel plate was heated to 27.4 °C through the application of a thermal energy pulse. Thermograms were captured on the same side at a frequency of 0.02 seconds for 5 min. The images of the thinned surface were processed in two steps. First, the peak contrast time algorithm was used to estimate the residual thickness. Second, Gaussian adaptive thresholding was used to estimate the size of the holes. The maximum observable defects had a diameter of 5 mm and a residual thickness of 3 mm. The type of defect interface (steel–sand or steel–air) had no significant effect on the estimation of residual thickness or size. This study developed a rapid approach in classifying defect's residual thickness by only utilizing two well-known parameters from infrared images – defect's peak thermal contrast and estimated area. Thus, the feasibility of non-destructive, in-pipe, quantitative IR thermographic analysis of buried metal pipelines is demonstrated.

Key words: Infrared thermography, residual thickness estimation, size estimation, Peak Thermal Contrast, Peak Contrast Time, Adaptive Thresholding

1. Introduction

1.1. Background

Many utilities, including water mains, gas mains, foul sewers, and telecommunication cables, are buried under every metropolis. These utilities are essential to the city; however, like all infrastructure, they deteriorate and have limited-service lifespans. Failures occur due to prolonged deterioration, which result in enormous social and economic costs. Thus, it is essential that the condition of underground utilities is periodically assessed.

Underground utilities fail for a variety of reasons, including internal and external corrosion. External corrosion of pipe walls is the principal cause of pipe failures. Its occurrence is mainly due to the leakage of water from surrounding utilities and corrosive soil material, which accelerate the oxidation and corrosion processes [1]. Corrosion continues until pit holes are formed, at which point leakage occurs. Pipe wall thinning due to corrosion can also create cracks in the pipe; at a certain point, the pipe will not be thick enough to withstand the high internal pressure of water or gas. There is no reliable technique for the in-situ monitoring of pipeline conditions, especially for the corrosion of pipe walls in unfavourable soil conditions. Traditional visual inspection using closed-circuit television can only assess the internal condition of the pipe, not the thinning of the external wall. Thermography (infrared thermal imaging) may overcome these limitations to enable the diagnosis of external pipe wall conditions.

Infrared thermal thermography was initially developed for the evaluation of

delamination in composite materials [2-5]. However, it is a highly developed tool that is now used in research and development in many fields. Spurred by technological advancements and the growth of the camera manufacturing industry, thermography has found applications in condition monitoring for existing infrastructure, predictive maintenance, and non-destructive testing. It is especially useful in the detection of unseen delamination in a wide range of composite materials, such as carbon and glass fibre-reinforced polymers [3, 6-8]. In the past few years, active thermography for non-destructive testing (TNDT) has been applied to spacecraft structures, building facades and underground utilities, where it has been used to survey conditions and assess in-pipe liners [9]. Through the use of TNDT, the direct and indirect costs of open-trench pipeline investigations can be reduced.

Active thermography relies on the controlled penetration of energy into a sample to reveal deep-lying defects. Different types of thermography exert energy for different durations. Pulsed thermography is the most commonly used type for quantitative analysis because it allows the infrared (IR) camera to rapidly record the thermal changes at the sample surface [10, 11].

Defect depth and residual thickness are two parameters that need to be resolved to characterise a defect. Many reports describe a positive relationship between defect depth, residual thickness, and the specific characteristic time of the inspected surface; however, most of these reports only consider defects at the sample–air interface [5, 11-18]. Externally corroded walls in buried pipes are not usually located at the sample–air interface. In this case, a sample–sand interface would be a more suitable model. Zeng, et al. [14] investigated the effect of non-air interfaces in the estimation of residual thickness. Using the peak contrast time (PCT) method, they showed that the interface material (water, wax or oil) influences the measurement. However, their experiment only focused on two shallow defects.

Size is another parameter that should be addressed when characterizing subsurface defects [2, 5, 9, 17, 19-21]. However, there are few studies on the effect of defect interface on size estimation on the evaluation of subsurface defects. Due to the fact that underground utilities are buried beneath the surface, the effect of unique interface (steel-sand interface) is vital to be explored. This study evaluated the feasibility of pulsed thermography, a TNDT method, for the rapid assessment of buried metal pipelines, with an emphasis on the estimation of residual thickness and defect size. A mild steel sample with 11 flat-bottomed holes, which were milled with different residual thicknesses and diameters, was analysed at the interface with air and sand. The estimated size and residual thickness of the holes were compared at the two interfaces.

2. Basic Theory

2.1. Pulsed thermography

Pulsed thermography is a commonly used TNDT method. As shown in Fig. 1, the specimen surface is briefly excited with a short pulse of thermal energy and an IR camera records the temporal temperature change at the surface. The location of subsurface defects can be determined from the temperature distribution [5, 19] ; any discontinuity in thermal properties due to subsurface defects will be evident from the surface temperature of the specimen after thermal excitation, as such discontinuities change the diffusion rate. When the thermal energy that propagates within the material reaches the defect, it is partially or wholly obstructed. Thus, an increase in temperature is observed at the surface above the defect with respect to the surrounding intact area.

For a defect free semi-infinite sample under instantaneous pulse, the one-dimensional solution [5, 19, 22] is:

$$T_{Surf}(0) = \frac{Q}{e\sqrt{\pi t}} \quad (1)$$

where Q is the input energy per unit area, t is the time after excitation and e is the thermal effusivity of the sample material, which is the square root of the product of thermal conductivity (κ), density (ρ) and the specific heat capacity (c) of the sample material. When there is a change in thermal properties, the one dimensional solution under instantaneous pulse [19] is:

$$T_{Surf}(0) = \frac{Q}{e\sqrt{\pi t}}[1 + 2\sum_{n=1}^{\infty} R^n \exp\left(\frac{-n^2 L^2}{\alpha t}\right)] \quad (2)$$

where L is the residual thickness of the defect area, t is the time after excitation, n is the number of energy reflections from the material discontinuity, α is the thermal diffusivity and R is the thermal mismatch factor. R is determined by the thermal effusivity of the sample and the defect. It is calculated as [19]:

$$R = \frac{e_1 - e_2}{e_1 + e_2} \quad (3)$$

where e_1 and e_2 are the thermal effusivity of the sample and the material behind the sample, respectively. For regions with subsurface defects, the effusivity of the defect will change the thermal mismatch factor, thus affecting the surface temperature of the region. Therefore, different defect interfaces theoretically result in different surface temperatures. However, the effect of defect interfaces had not been explored in-depth in the past and even for study that explored the effect of defect interfaces, their study focuses on interface of water and oil with uniform defect size and very small residual thickness [14]. Therefore, to fit in the case of underground metallic utilities, experiment is needed.

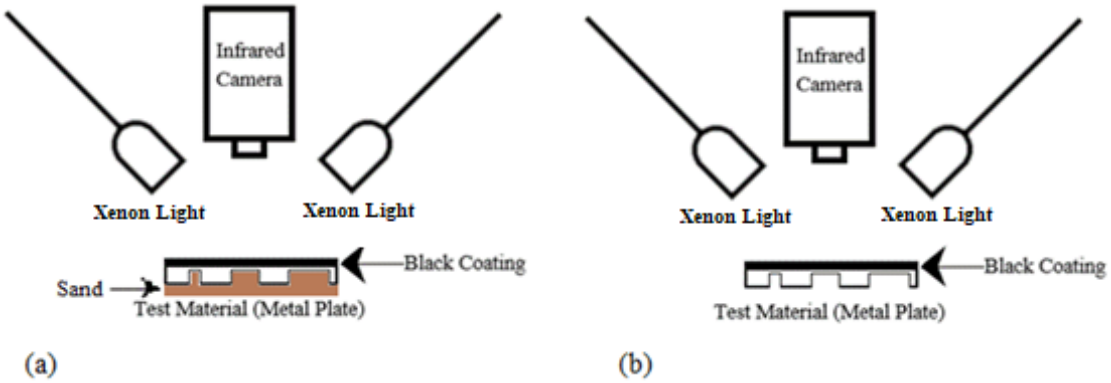

Fig. 1. Schematic diagram of the pulsed thermography set-up at (a) the steel–sand interface with an 86mm thick sand layer and (b) the steel–air interface

2.2. Defect Residual Thickness Estimation

The estimation of residual thickness is important in the characterisation of subsurface defects. The visibility of subsurface defects on the thermogram is enhanced by temperature contrast. Because intact areas and defect areas behave differently after excitation, temperature contrast enables the residual thickness of the defect to be obtained. Temperature contrast is calculated as follows [5, 19, 22]:

$$C(t) = T_{def}(t) - T_{sound}(t) \quad (4)$$

where T is the temperature signal, t is the lapsed time, and *def* and *sound* refer to areas with a suspected defect and sound areas, respectively. Areas with suspected defects display thermal anomalies. Intact areas are defined as regions that are close to a thermal anomaly, but do not themselves display an anomaly. When the thermal energy that propagates from the surface reaches near-surface defects, it is reflected back to the surface. Therefore, the time of maximum thermal contrast is delayed for deeper defects compared with shallower defects. The time of maximum thermal contrast is an effective measure for the estimation of residual thickness.

2.3. Multi-Dimensional Heat Transfer

The quantification of defect area, unlike depth, requires a three-dimensional analysis of heat transfer. The one-dimensional heat transfer pattern described in 2.1 becomes more complex when extended to two dimensions.

The thermal responses of any object can be described by a differential form of three-dimensional heat conduction, as described by the following equation [19]:

$$C\rho\frac{\partial T}{\partial t} = \frac{\partial}{\partial x}\left(k_x\frac{\partial T}{\partial x}\right) + \frac{\partial}{\partial y}\left(k_y\frac{\partial T}{\partial y}\right) + \frac{\partial}{\partial z}\left(k_z\frac{\partial T}{\partial z}\right) + w(x,y,z) \quad (5)$$

where C is specific heat capacity ($\mathrm{J\,kg^{-1}K^{-1}}$), ρ is the density ($\mathrm{kg\,m^{-3}}$), T is the temperature (K), t is the lapsed time (s), k_x, k_y, k_z ($\mathrm{W\,m^{-1}K^{-1}}$) are the anisotropic thermal conductivities in the three principal directions of heat transfer in the material and $w(x,y,z)$ is the rate of energy generation per unit volume in the medium. If the object does not generate heat by itself, Eq. 5 can be simplified into the following form:

$$C\rho\frac{\partial T}{\partial t} = \frac{\partial}{\partial x}\left(k_x\frac{\partial T}{\partial x}\right) + \frac{\partial}{\partial y}\left(k_y\frac{\partial T}{\partial y}\right) + \frac{\partial}{\partial z}\left(k_z\frac{\partial T}{\partial z}\right) \quad (6)$$

Thermal diffusivity (α) may be expressed in terms of thermal conductivity (k), specific heat capacity (C) and density (ρ), as follows:

$$\alpha = k(C\rho)^{-1} \quad (7)$$

Thus, if the material's thermal conductivity remains the same in all three principal directions, that is $k_x = k_y = k_z$, Eq. 6 can be expressed as follows:

$$\frac{\partial^2 T}{\partial x^2} + \frac{\partial^2 T}{\partial y^2} + \frac{\partial^2 T}{\partial z^2} = \frac{1}{\alpha}\frac{\partial T}{\partial t} \quad (8)$$

Eq. 6 and 8*(8)* distinguish how defective and sound areas behave differently with time after excitation. Eq. 6 describes the behaviour of defect areas. A Gaussian-like thermal energy distribution results from the heterogeneity of the thermal properties of the defect, as described in section 2.1. Eq. 8 describes the isotropic thermal behaviour of sound areas by depicting a uniform temperature distribution on the surface of the object. For externally corroded underground utilities modelled in Fig. 1, the difference between the thermal properties, including thermal conductivity and heat capacity, of the buried metallic pipe and the surrounding soil create a high of effusivity difference leading to a high thermal mismatch factor which allows for intact and defective areas to be readily distinguished.

2.4. Defect Size Estimation

Methods for the estimation of the size of subsurface defects can be divided into two categories: (1) those that use surface profile of thermogram [2, 17, 19, 23, 24] and (2) those that use thresholding techniques [5, 9, 20, 21, 25-27].

Methods that utilise thermogram surface profiles are based on the theoretical principle described in section 2.3. This group of methods includes the full width at half maximum (FWHM) method and the pixel differentiation method. The FWHM method for defect size estimation has been applied on phasegrams from optical beam deflection thermal wave systems (since 1982) [23] and on time-domain temperature profiles of transient thermography (since 1994) [24]. This method determines the size of defects by locating the pixel that is equal to the halved value of the maximum temperature along a cross-section of the thermogram of the suspected defect. The pixel differentiation method is similar to the FWHM method; however, it utilises Eq. 2 and 3 to define the edges of the defect, as the edges should have maximum thermal contrast [2].

These methods require considerable processing work because every profile within the thermogram must be analysed, and in both x and y directions. Thresholding techniques, in contrast, can provide a swift estimate of defect size by binarising pixels on the thermogram based on a selected threshold. These thresholds can be either typical statistical thresholds [21, 25, 26] or thresholds that are dedicated to the characteristics of the heat transfer mechanism [20, 27]. The current study aims to rapidly detect defective and sound regions. Therefore, a statistical thresholding technique – adaptive Gaussian weighted mean thresholding, also known as adaptive thresholding – is used.

The adaptive Gaussian weighted mean defines a local threshold for a selected region to undergo binarisation. The algorithm is expressed as follows:

$$\bar{T} = \frac{\sum_{i=1}^{n} w_i T_i}{\sum_{i=1}^{n} w_i} \tag{9}$$

where T_i is the pixel intensity (counts) and $\bar{T}$ is the mean intensity of the selected region. Normally, if $T_i > \bar{T}$, the pixel is defined as a defect, and if $T_i < \bar{T}$, the pixel is defined as a background signal. However, after the weighted mean pixel value of the region is calculated, it is normally multiplied by a manually defined percentage value, p. If the pixel is p per cent larger than the weighted mean pixel value, then it is classified as a defect, and otherwise it is defined as background [28]. Thus, more pixels will be classified as defects as the p value increases. In this paper, the p value is set at 5% with empirical testing using one defect as reference and minimizing the difference between the estimated area and actual area. This minimises the number of pixels that are classified as defects, but also accounts for the potential effect of random noise. After classifying the pixels, the actual size of the defect can be estimated using the distance between the IR camera and the object and the instantaneous field of view (IFOV) of the camera image by:

$$IFOV_{img} = Distance \times IFOV$$

where IFOV is obtained from either the camera specifications or with the following equation Maldague [22], [29]:

$$IFOV = (HFOV/number\ of\ pixels) \times 3.14/180 \times 1000$$

3. Material and Instrumentation

3.1. Test sample

The setup for the adapted pulsed thermography is shown in Fig. 1. Sequential IR image data were obtained using a pulsed-heating TNDT system. In this experiment, a 150

mm (length) × 150 mm (width) × 10 mm (thick) mild steel plate was machine-milled with 11 flat-bottom holes. The holes had varying diameters (20 mm, 15 mm, 10 mm, 5 mm) and residual thicknesses (1 mm, 3 mm, 5 mm) to imitate the various defects in a pipe wall. To model the environment of a buried metallic pipe, several sets of data were collected while the holes were filled with sand. A schematic illustration of the steel plate is shown in Fig. 2.

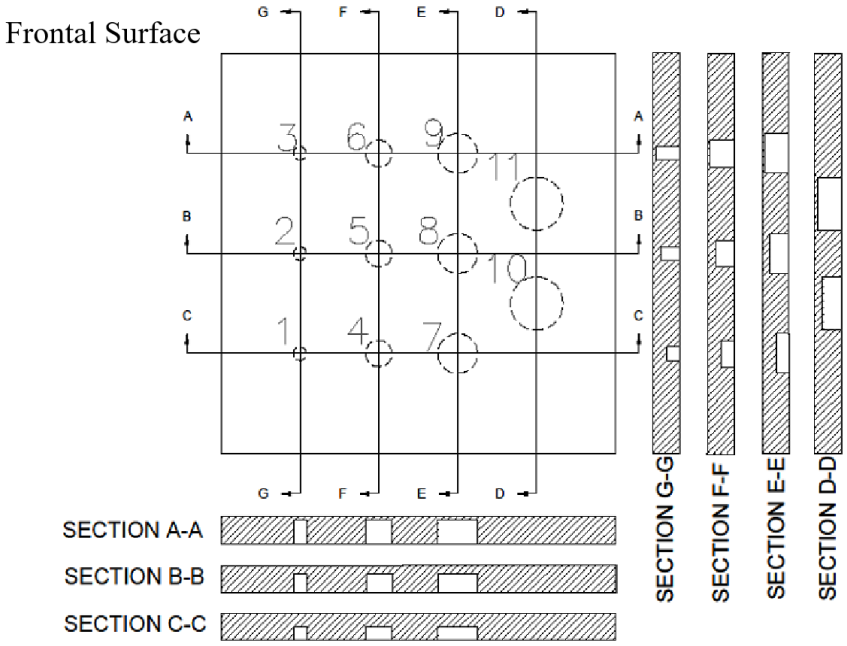

No.	1	2	3	4	5	6	7	8	9	10	11
Diameter (mm)	5			10			15			20	
Residual Thickness (mm)	5	3	1	5	3	1	5	3	1	3	1

Fig. 2. Schematic diagram of the mild steel sample with machined flat-bottom holes and a table of geometric data.

3.2. Instrumentation

A pair of flash lamps, which were directed towards the rear surface of the plate, was used for excitation (at t = 0 s). The plate was painted with a thin layer of black flat paint so that its emissivity was as close as possible to that of a blackbody. The change in temperature of the surface was monitored by a high-speed, long-wave infrared camera (7–14 μm) with a 640 × 480 pixel microbolometer at a frame rate of 50 Hz for 5 minutes after the application of the pulse. The instrument specifications and parameters used for the acquisition of the thermogram are provided in Table 1.

Table 1. Experimental equipment and acquisition parameters.

Experimental Equipment	**Acquisition Parameters**	
Thermal stimulation:	Sampling rate	50 Hz
Photographic Flashes: ELINCHROM ZOOM Pro HD Pulse duration: 4 ms thermal pulse, Deposited energy: 3 kJ/flash (Total energy deposited 6 kJ)	Acquisition duration	156 s
Thermographic monitoring	Time interval	20 ms

FLIR A655sc, FOV 25°, 640 × 480 pixel microbolometer, 16-bit data, NETD: <30 mK, spectral range: 7.5-14.0 μm	Total number of frames 7800

4. Results and Discussion

Six sets of flash thermographic data were collected; three at the steel–air interface and three at the steel–sand interface. The thermograms at the steel–air interface, shown in Fig. 3(a), depict the surface temperature of the plate 1 second after excitation. Defects with lower residual thickness and larger sizes yielded higher temperatures. The visibility limit is reached at defect 2, which has a residual thickness of 3 mm and a diameter of 5 mm. In addition, the thermal contrast is better at the edges of defects with lower residual thickness than at those with higher residual thickness. Adaptive thresholding, using Eq. 8 (refer to section 2.4), was applied to each level of residual thickness within the image. Defects are classified by the grey-scale temperature values, which are strongly correlated with the residual thickness. Using the largest defect as a reference, a threshold sensitivity level (*p* value) of 5% is able to differentiate the residual thickness. As a result, defects with a residual thickness of 1 mm, 3 mm and 5 mm are masked separately. A sample of the binary image obtained using an empirical sensitivity level (*p* value) of 5% for defects with a 1 mm residual thickness is depicted in Fig. 3(b). The temperature decay curves after the pulse are shown on a natural log scale in Fig. 4. Each defect on the sample plate was acquired and compared with a sound area next to the defect to obtain the contrast temperature curve. The contrast temperature curve, processed with Eq. 4, is shown in Fig. 5.

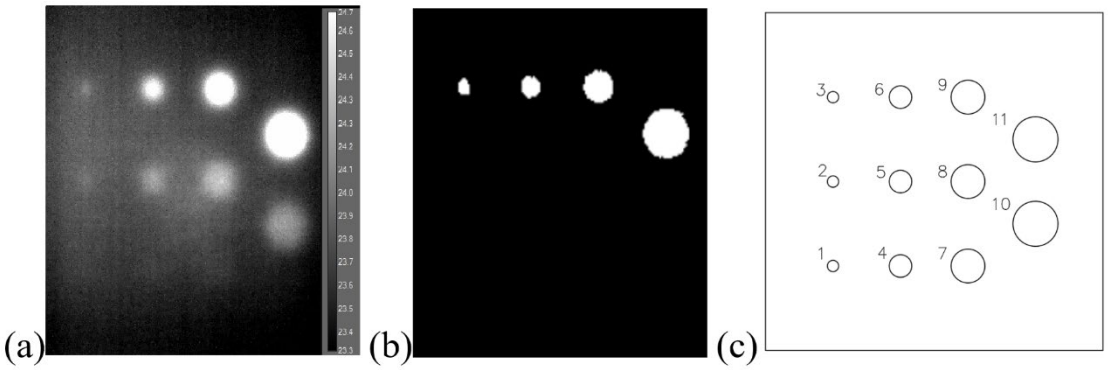

Fig. 3. (a) Raw infrared thermogram at 1 s after pulse with colour bar set between 23.3℃ - 24.7℃; (b) Binary image generated by Gaussian adaptive thresholding with a sensitivity level (*p* value) of 5% on defects with 1 mm residual thickness, and (c) the sample steel plate for defect referencing.

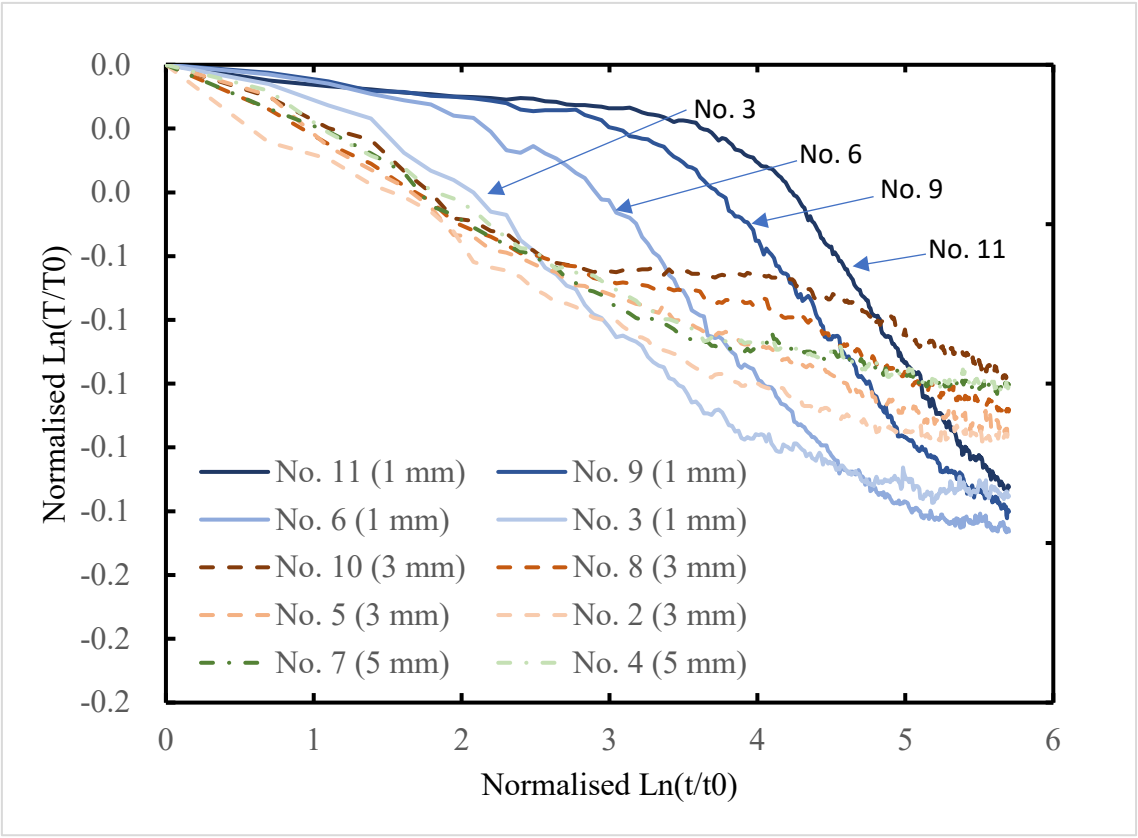

Fig. 4. A set of experimental temperature curves of the mild steel sample.

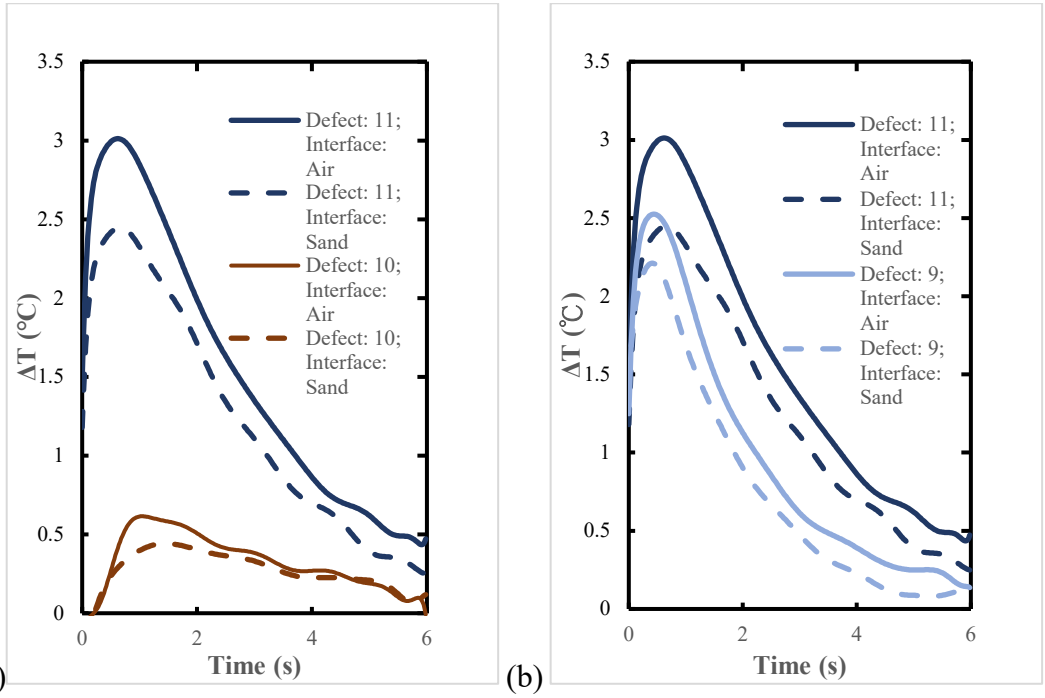

Fig. 5. Contrast-time curves at the steel–air interface and steel–sand interface for (a) defects with the same sizes but different residual thickness, and (b) defects with the same residual thickness but different defect sizes.

4.1. Residual Thickness Estimation with Peak Contrast Time Method

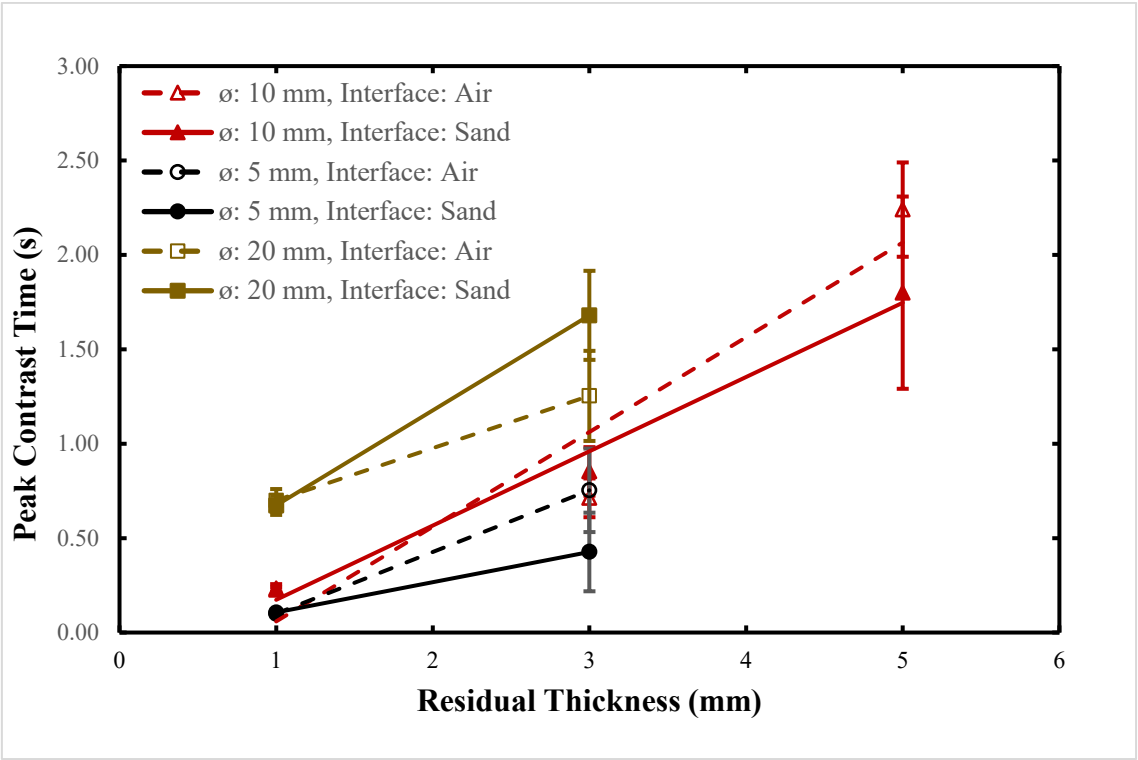

Fig. 6. PCT of steel–air interface and steel–sand interfaces versus residual thickness of defect samples.

After the energy pulse was applied to the sample surface, deeper defects tended to reach peak values at a later stage, as shown in Fig. 5 and Fig. 6. However, from Fig. 6, it can be observed that the interface material has a minimal effect (< 0.1 °C) on defects with 1 mm residual thickness and a larger effect (> 0.5 °C) on defects with greater residual thickness. A similar trend can be seen in Fig. 7.

For defects with a diameter of 20 mm, those with larger residual thickness are more sensitive to the interface. The differences in PCT between the steel–air and steel–sand interfaces for defects with 1 mm residual thickness are larger than those of defects with 5 mm residual thickness. The sensitivity to the interface material is also dependent on the diameter of the defect. The difference in PCT between the steel–air and steel–sand interface for defects of differing diameters is shown in Fig. 7. It can be seen that the diameter is positively correlated with PCT for defects with a depth of 3 mm.

In summary, the PCT depends not only on the residual thickness and diameter of the defect but also on the material at the interface. Both the residual thickness and diameter determine the effect that the interface material has on the PCT. As shown in Fig. 5 – Fig. 7, the residual thickness of the defect has the largest influence on the peak thermal contrast and PCT, and the type of interface has the smallest influence. Therefore, the evaluation of the residual thickness should be prioritised when using the PCT method in IR thermography for the assessment of defects in underground utilities.

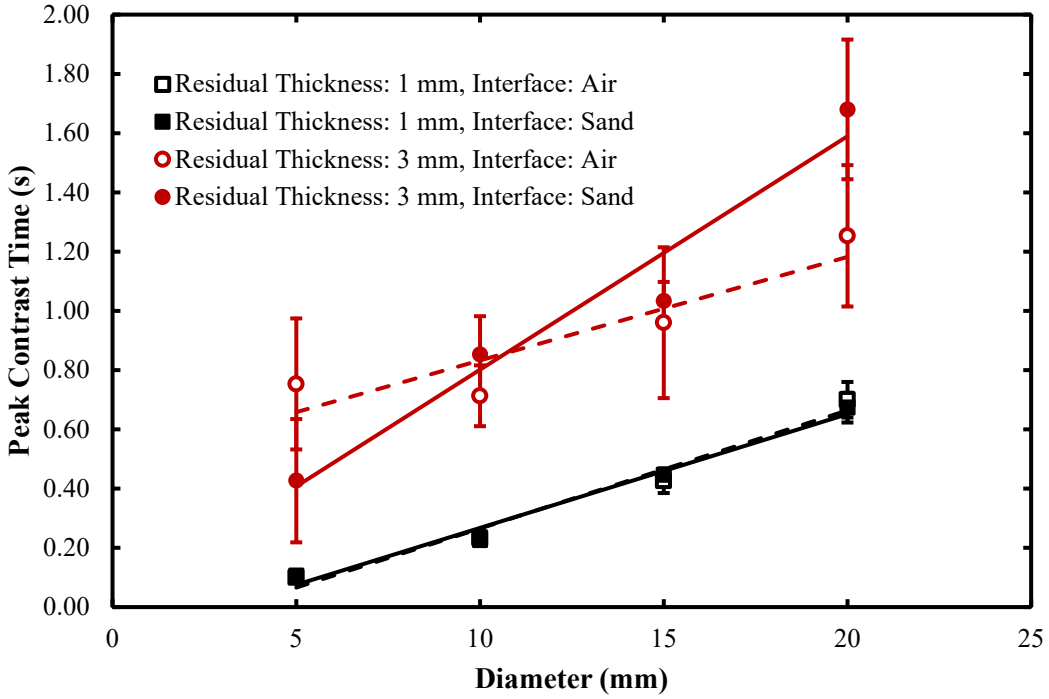

Fig. 7. PCT of steel-air interface and steel-sand interface against diameter of defect samples.

4.2. Size Estimation with Gaussian Adaptive Thresholding

The estimation of size is more accurate for defects with lower residual thickness; the size of defects with greater residual thickness is underestimated. As shown in Fig. 8, the linear correlation between the measured and actual defect areas is better for defects with 1 mm depth than for those with 3 mm depth, at both the steel–air and steel–sand interfaces. At the steel–air interface, the average difference between the estimated and actual sizes is -0.45% for defects with 1 mm residual thickness and -25.2% for defects with 3 mm residual thickness. At the steel–sand interface, the difference is -13.2% for defects with 1 mm residual thickness and -23.1% for defects with 3 mm residual thickness.

Thermal energy diffuses in three dimensions, as described in Eq. 6 and 8. For defects with greater residual thickness, the thermal energy must travel for longer in the z-direction to reach the opposite side of the material. At the same time, more thermal energy diffuses into surrounding areas in the x- and y-directions. Thus, less thermal energy reaches the excited surface after reflection from the defect interface. This creates a gentle slope of temperature variation on the object's surface. Defects with larger residual thickness therefore tend to have lower pixel values and blurrier defect edges, which results in less accurate size estimations.

The difference between the estimated and actual size is inversely related to the defect diameter. As shown in Fig. 9, the size estimation error decreases from an average of 5.25% for a diameter of 5 mm to -3.5% for a diameter of 20 mm.

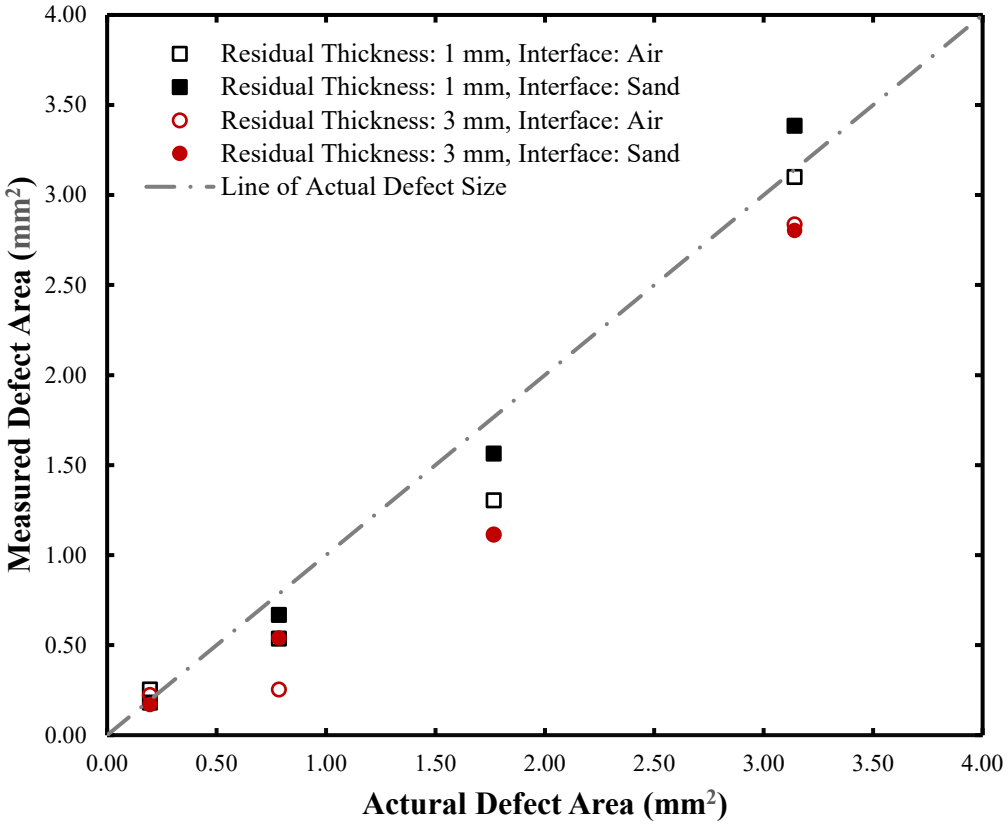

Fig. 8. Estimated defect size (using Gaussian adaptive thresholding) versus actual size.

Even though most of the defect size using gaussian adaptive thresholding of same sensitivity are underestimated, there is no significant differences in estimating the size of defect between steel-sand interface and steel-air interface for shallow defects since the result of thresholding method is calculated by surface temperature of the sample, which depends on the thermal mismatch value of the interface and thermal conductivity of the sample. Although sand-filled interface is physically different from air-filled interface, the thermal properties of sand and air are similar as sand-filled interface contains air gaps within sand particles. Thus, their thermal properties are similar resulting in similar mismatch factor. Similarly, in terms of conductivity, although sand behind the thinned area has a higher thermal conductivity that conducts more energy from the steel plates than that of air resulted in a reduction of reflected thermal energy, such effect is insignificant compared with the effect of residual thickness. By comparing the percentage difference of 1mm deep defect, both interfaces resulted in similar size discrepancy with a difference of 0.73% where the average percentage difference in size of all 1mm defects for steel-sand interface is -6.82% and the average percentage difference in size of 1mm defects for steel-air interface is -7.55%. The effect of interface differences becomes more noticeable in defect with larger residual thickness. The average percentage difference in size increased from -25.2% at 1mm residual thickness to -23.1% at 3mm residual thickness. Although this increase in difference due to interface material changes is observable, it is not noticeable.

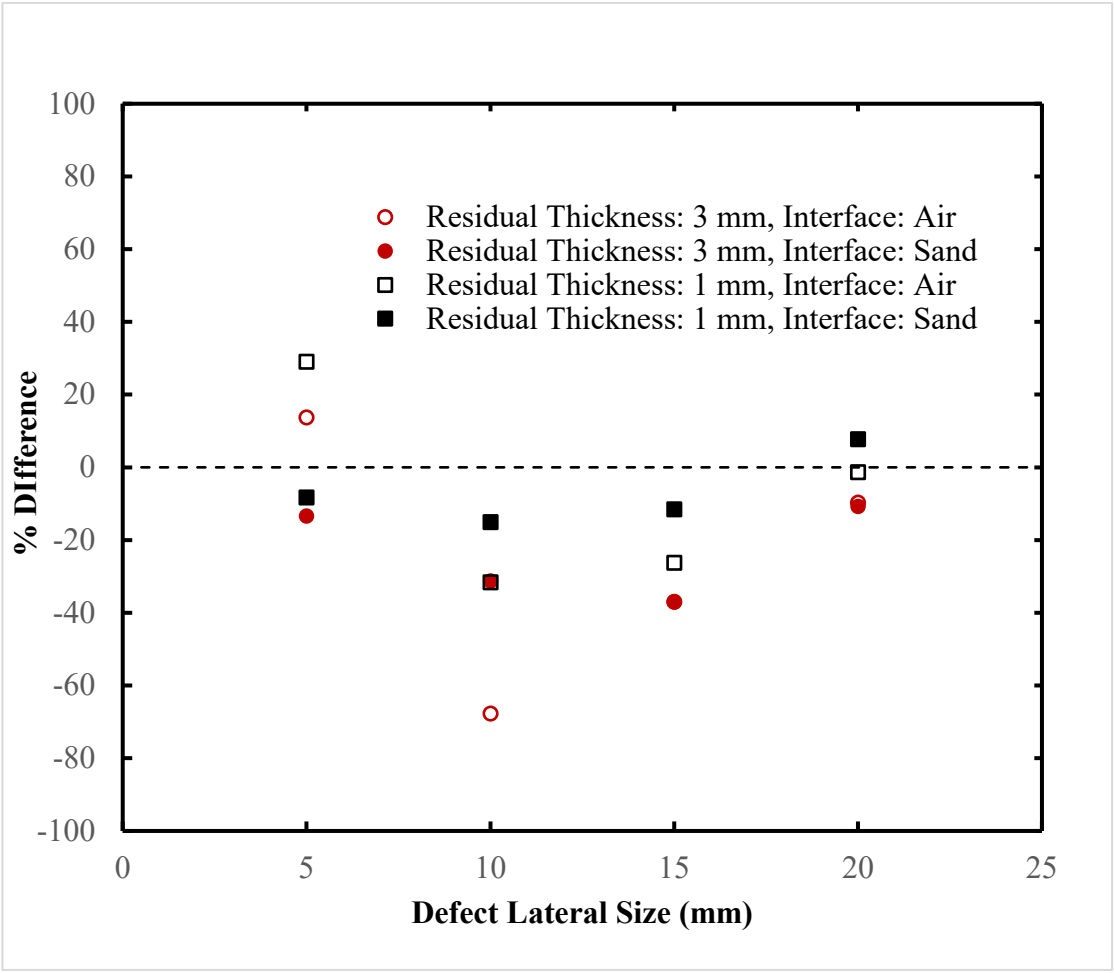

Fig. 9. Percentage difference between estimated and actual size versus defect diameter.

4.3. Effect of Sand on Thermal Contrast

For defects with a 1 mm residual thickness, the peak thermal contrast is generally lower at the steel–sand interface than at the steel–air interface, while this is reversed for defects with a 3 mm residual thickness (Fig. 5, Fig. 10 and Fig. 11); however, these differences are not significant. The largest average difference in thermal contrast is only 0.5 °C (for defects with a residual thickness of 1 mm and diameter of 20 mm, Fig. 10). The difference in thermal contrast between the two interfaces generally increases with increasing defect size as shown in Figs. **10** and **11**. The thermal contrast for defects with low residual thickness is only slightly affected by the material at the interface. Although sand has a higher thermal conductivity than air, which results in less reflection of thermal energy at the interface, this effect is not significant. In addition, for defects with greater residual thickness, the thermal energy diffuses in other directions immediately after the excitation pulse due to the higher thermal conductivity of steel; thus, the effect of the interface is minimal. As aforementioned the thermal properties of sand and air are similar as sand-filled interface contains air gaps within sand particles, the R value of steel–air or steel–sand interface will be similar. Thus, no significant impact could be observed. The maximum thermal contrast values at the sand–steel interface have a lower standard deviation than those at the sand–air interface. However, the magnitude of this difference is not significant when classifying the residual thickness of the metal plate.

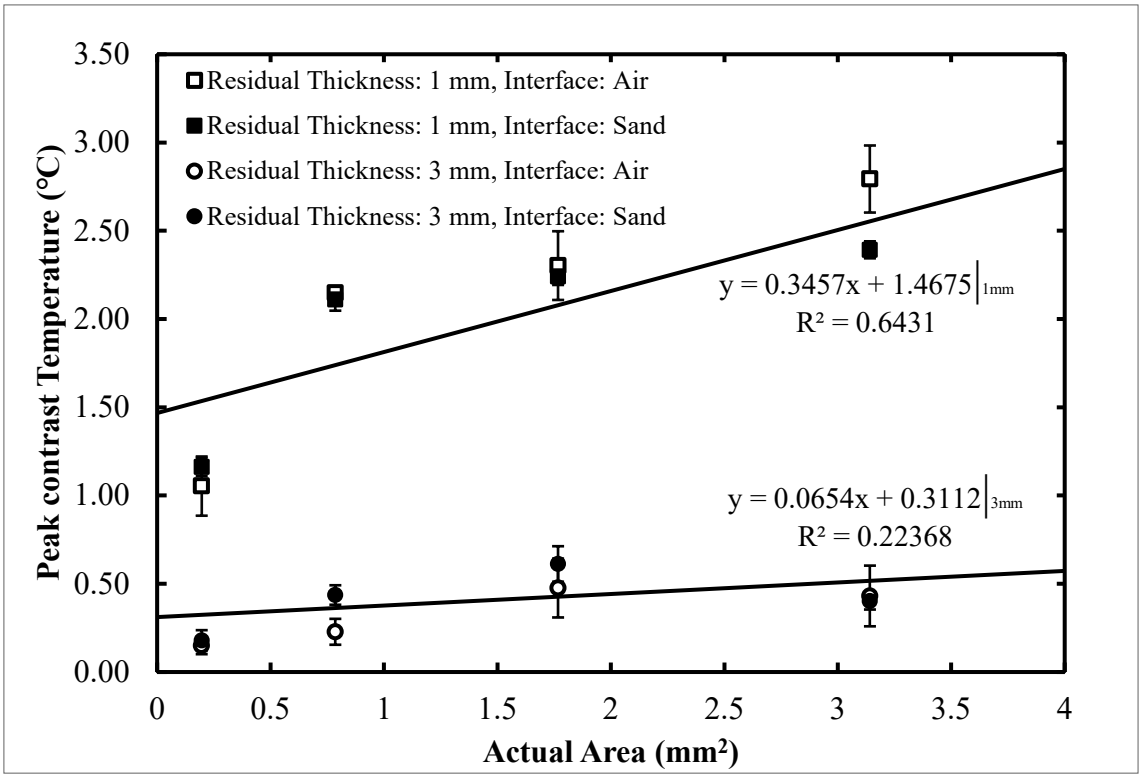

339

340 **Fig. 10**. Peak thermal contrast versus actual defect diameter. The error bars indicate 1
341 standard deviation of 3 replicate measurements.
342

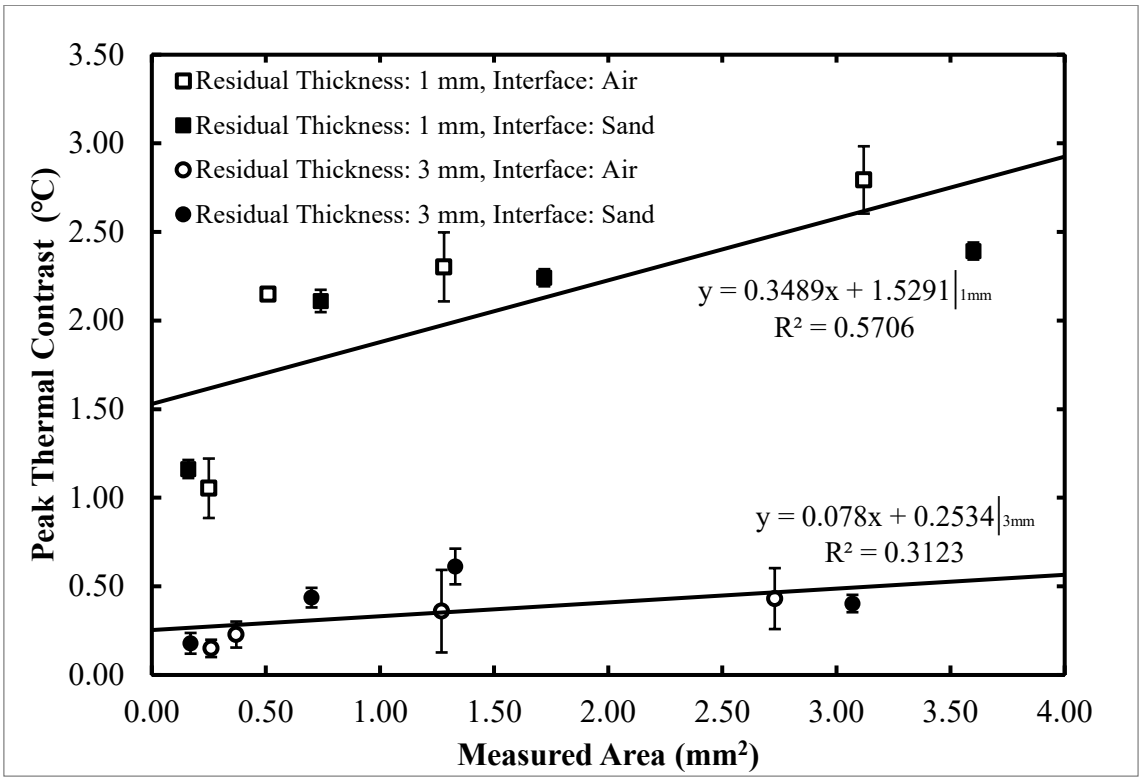

343

344 **Fig. 11.** Plot of peak contrast temperature verses measured defect area with error bar
345 determined by the standard deviation 3 replicate measurements.

4.4. Classification of Defects with no Prior Knowledge

Fig. 10 and Fig. 11 illustrates the feasibility of classification of defects using peak thermal contrast with no prior knowledge of the specimen. Fig. 10 illustrates how data would be presented if the observer having prior knowledge of the specimen where data are organized by the prior knowledge of defect size. On the other hand, Fig. 11 illustrates how data would be presented if the observer does not have any prior knowledge of the specimen. Despite the difference in the method of presenting the data, they depicted similar results which was shown by their R-squared value. From both figures, defects with 1 mm residual thickness have a R-squared value of around 0.6 while defects with 3 mm residual thickness have a R-squared value of around 0.3. This implies that by only having defects' measured size and its peak thermal contrast, defects can be classified into different residual thickness group. This implication demonstrated that conducting in-pipe condition assessment would be possible since most underground utilities were not able to be exposed to conduct condition assessment externally which the defect size is unknown to the assessor. Knowing that classification of defects does not requires prior knowledge allows utility stakeholders utilizing IR technology for in-pipe condition assessment.

5. Conclusion

In this study, we used pulsed thermography to analyse the effects of defect size, residual thickness, and interface material on thermal behaviour within a steel sample. The results indicate that pulsed thermography can clearly reveal defects with residual thicknesses of up to 3 mm and diameters of up to 5 mm. The residual thickness and size of the defect significantly affect the thermal behaviour. However, the interface material does not significantly affect the thermal behaviour; thus, the characterisation of defects (in terms of size and residual thickness) is not affected. Similarly, interface material has observable, but insignificant, effects on the estimation of defect size using Gaussian adaptive thresholding techniques. This study delineates the importance of validating the effects of residual defect thickness, defect size, and interface material on the thermal behaviour of specific materials during IR thermography. Based on the validation, this study developed a rapid approach in quantifying and classifying defects' residual thickness by utilizing only defects' estimated size and their corresponding peak thermal contrast. This study depicted how defects would be illustrated under the condition of assessor not having prior knowledge of the specimen and its implication on how IR technology is feasible for conduction underground utility in-pipe assessment. This study focuses on the issue of identification and quantification of defects with steel-sand interface due to the unique environment of buried underground structures. However, the issue of soil characteristics, compactivity and wetness are not explored. Future research could focus on such issue to provide a more comprehensive understanding of how soil condition affects the result of IR thermography. Our future work will also include the investigation of other heating methods and testing IR technology on real pipeline.

Acknowledgements

The authors gratefully acknowledge the Hong Kong and China Gas Company Limited and the Innovation Technology Commission of the Government of the HKSAR for funding support.

Reference

[1] M. Wasim, S. Shoaib, N. M. Mubarak, Inamuddin, and A. M. Asiri, "Factors influencing corrosion of metal pipes in soils," *Environmental chemistry letters,* vol. 16, no. 3, pp. 861-879, 2018, doi: 10.1007/s10311-018-0731-x.

[2] W. W.-L. Lai, K.-K. Lee, and C.-S. Poon, "Validation of size estimation of debonds in external wall's composite finishes via passive Infrared thermography and a gradient algorithm," *Construction and Building Materials,* vol. 87, pp. 113-124, 2015/07/15/ 2015, doi: 10.1016/j.conbuildmat.2015.03.032.

[3] D. J. Titman, "Applications of thermography in non-destructive testing of structures," *NDT & E International,* vol. 34, no. 2, pp. 149-154, 2001/03/01 2001, doi: 10.1016/S0963-8695(00)00039-6.

[4] G. A. Washer, "Developments for the non-destructive evaluation of highway bridges in the USA," *NDT & E International,* vol. 31, no. 4, pp. 245-249, 1998/08/01/ 1998, doi: https://doi.org/10.1016/S0963-8695(98)00009-7.

[5] X. Maldague, *Theory and practice of infrared technology for nondestructive testing*. New York: Wiley, 2001.

[6] M. Vollmer, *Infrared thermal imaging : fundamentals, research and applications*, Second edition.. ed. Weinheim: Weinheim : Wiley-VCH, 2018.

[7] F. Ciampa, P. Mahmoodi, F. Pinto, and M. Meo, "Recent Advances in Active Infrared Thermography for Non-Destructive Testing of Aerospace Components," *Sensors,* vol. 18, no. 2, p. 609, 2018. [Online]. Available: https://www.mdpi.com/1424-8220/18/2/609.

[8] F. C. Sham, N. Chen, and L. Long, "Surface crack detection by flash thermography on concrete surface," *Insight - Non-Destructive Testing and Condition Monitoring,* vol. 50, no. 5, pp. 240-243, 2008, doi: https://doi.org/10.1784/insi.2008.50.5.240.

[9] J. F. C. Sham, W. W. L. Lai, W. Chan, and C. L. Koh, "Imaging and condition diagnosis of underground sewer liners via active and passive infrared thermography: A case study in Singapore," *Tunnelling and Underground Space Technology,* vol. 84, pp. 440-450, 2019/02/01/ 2019, doi: https://doi.org/10.1016/j.tust.2018.11.013.

[10] J. Erazo-Aux, H. Loaiza-Correa, A. D. Restrepo-Giron, C. Ibarra-Castanedo, and X. Maldague, "Thermal imaging dataset from composite material academic samples inspected by pulsed thermography," *Data in Brief,* vol. 32, p. 106313, 2020/10/01/ 2020, doi: 10.1016/j.dib.2020.106313.

[11] P. Theodorakeas and M. Koui, "Depth Retrieval Procedures in Pulsed Thermography: Remarks in Time and Frequency Domain Analyses," *Applied*

Sciences, vol. 8, no. 3, p. 409, 2018. [Online]. Available: https://www.mdpi.com/2076-3417/8/3/409.

[12] Z. Zeng, J. Zhou, N. Tao, L. Feng, and C. Zhang, "Absolute peak slope time based thickness measurement using pulsed thermography," *Infrared Physics & Technology,* vol. 55, no. 2, pp. 200-204, 2012/03/01 2012, doi: 10.1016/j.infrared.2012.01.005.

[13] H. D. Benítez, C. Ibarra-Castanedo, A. Bendada, X. Maldague, H. Loaiza, and E. Caicedo, "Definition of a new thermal contrast and pulse correction for defect quantification in pulsed thermography," *Infrared Physics & Technology,* vol. 51, no. 3, pp. 160-167, 2008/01/01/ 2008, doi: https://doi.org/10.1016/j.infrared.2007.01.001.

[14] Z. Zeng, C. Li, N. Tao, L. Feng, and C. Zhang, "Depth prediction of non-air interface defect using pulsed thermography," *NDT & E International,* vol. 48, pp. 39-45, 2012/06/01/ 2012, doi: https://doi.org/10.1016/j.ndteint.2012.02.008.

[15] J.-C. Krapez, F. Lepoutre, and D. Balageas, "Early detection of thermal contrast in pulsed stimulated thermography," *J. Phys. IV France,* vol. 04, no. C7, pp. C7-47-C7-50, 1994. [Online]. Available: https://doi.org/10.1051/jp4:1994712.

[16] X. Han, L. D. Favro, P. K. Kuo, and R. L. Thomas, "Early-Time Pulse-Echo Thermal Wave Imaging," *Symposium on Quantitative Nondestructive Evaluation San Diego, Calif,* pp. 519-524, 1996, doi: 10.1007/978-1-4613-0383-1_66.

[17] O. Wysocka-Fotek, W. Oliferuk, and M. Maj, "Reconstruction of size and depth of simulated defects in austenitic steel plate using pulsed infrared thermography," *Infrared Physics & Technology,* vol. 55, no. 4, pp. 363-367, 2012/07/01/ 2012, doi: https://doi.org/10.1016/j.infrared.2012.02.004.

[18] S. K. Lau, D. P. Almond, and J. M. Milne, "A quantitative analysis of pulsed video thermography," *NDT & E International,* vol. 24, no. 4, pp. 195-202, 1991/08/01/ 1991, doi: https://doi.org/10.1016/0963-8695(91)90267-7.

[19] X. Maldague and P. O. Moore, *Nondestructive Testing handbook, infrared and thermal testing*, 3rd ed. (Infrared and thermal testing). Columbus, OH: Columbus, OH : American Society for Nondestructive Testing, 2001.

[20] R. Heriansyah and S. Abu-Bakar, "Defect detection in thermal image using thresholding technique," in *6th WSEAS International Conference on Circuits, Systems, Electronics, Control & Signal Processing*, Cairo, Egypt, 2007, pp. 341-346.

[21] Z. Li, C. Liu, G. Liu, X. Yang, and Y. Cheng, "Statistical thresholding method for infrared images," *Pattern Analysis and Applications,* vol. 14, no. 2, pp. 109-126, 2011/05/01 2011, doi: https://doi.org/10.1007/s10044-010-0184-8.

[22] X. Maldague, *Nondestructive evaluation of materials by infrared thermography*. London, Hong Kong: Springer-Verlag (in English), 1993.

[23] G. C. W. Jr. and F. A. McDonald, "Subsurface-structure determination using photothermal laser-beam deflection," *Applied Physics Letters,* vol. 41, no. 10, pp. 926-928, 1982, doi: 10.1063/1.93338.

[24] D. P. Almond and S. K. Lau, "Defect sizing by transient thermography. I. An analytical treatment," *Journal of Physics D: Applied Physics,* vol. 27, no. 5, pp. 1063-1069, 1994/05/14 1994, doi: 10.1088/0022-3727/27/5/027.

[25] X. Maldague, J. C. Krapez, and D. Poussart, "Thermographic nondestructive evaluation (NDE): an algorithm for automatic defect extraction in infrared images," *IEEE Transactions on Systems, Man, and Cybernetics,* vol. 20, no. 3, pp. 722-725, 1990, doi: 10.1109/21.57287.

[26] S. Araki, H. Nomura, and N. Wakami, "Segmentation of thermal images using the fuzzy C-means algorithm," in *[Proceedings 1993] Second IEEE International Conference on Fuzzy Systems*, 28 March-1 April 1993 1993, pp. 719-724 vol.2, doi: 10.1109/FUZZY.1993.327400.

[27] J.-S. Chang, H.-Y. M. Liao, M.-K. Hor, J.-W. Hsieh, and M.-Y. Chern, "New automatic multi-level thresholding technique for segmentation of thermal images," *Image and Vision Computing,* vol. 15, no. 1, pp. 23-34, 1997/01/01/ 1997, doi: https://doi.org/10.1016/S0262-8856(96)01087-6.

[28] D. Bradley and G. Roth, "Adaptive thresholding using the integral image," *Journal of graphics tools,* vol. 12, no. 2, pp. 13-21, 2007.

[29] T. Pencheva, D. Pulov, B. Gyoch, and M. Nenkov, "Design of CCD Optical System for Thermal IR Spectral Region," in *2006 29th International Spring Seminar on Electronics Technology*, 10-14 May 2006 2006, pp. 173-178, doi: 10.1109/ISSE.2006.365380.